ACS APPLIED MATERIALS & INTERFACES

Letter

www.acsami.org

Hybrid Self-Assembly during Evaporation Enables Drop-on-Demand Thin Film Devices

J. William Boley,*[,†,§] Seok-Hee Hyun,[‡] Edward L. White,[†] David H. Thompson,[‡] and Rebecca K. Kramer*[,†]

[†]School of Mechanical Engineering, Purdue University, West Lafayette, Indiana 47907, United States

[‡]Department of Chemistry, Purdue University, West Lafayette, Indiana 47907, United States

Supporting Information

ABSTRACT: We propose and demonstrate a hybrid self-assembly process as the mechanism for producing strikingly uniform deposits from evaporating drops composed of cosolvents. This assembly process leverages both particle−fluid interactions to carry the particles to the drop surface and particle−interface interactions to assemble the particles into a uniform film. We anchor our results in a cosolvent evaporation model that agrees with our experimental observations. We further employ the process to produce thin film devices such as flexible broadband neutral density filters and semitransparent mirrors. Our observations suggest that this assembly process is free of particle−substrate interactions, which indicates that the results should be transferable across a multitude of material/substrate systems.

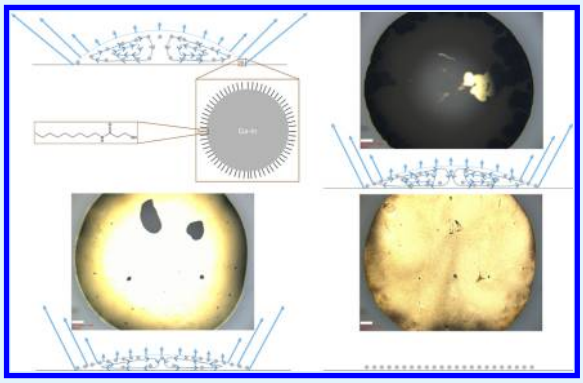

KEYWORDS: *liquid metal, gallium−indium, self-assembly, drop evaporation, cosolvent, monolayers, thin films, optics*

As a drop of liquid evaporates on a solid surface, the particles within form a deposit. Due to the myriad of physical and chemical processes involved during evaporation, the structure of this deposit can vary greatly, ranging from simple ring formations like those seen in coffee drops,[1] to more complex morphologies such as fractal patterns.[2,3] Of these possible outcomes, a strikingly uniform deposit may be formed by mixing together two cosolvents.[4,5] Although common wherever there are solvent mixtures (e.g., most kitchens, dining rooms, or pubs), these deposits also show great potential for industrial applications, as they may provide simpler, faster, and less costly ways to manufacture thin film devices compared to conventional methods.[6−9] By appropriately tuning design parameters, co-solvent-based deposits could also be used to produce conformal monolayer coatings on three-dimensional surfaces or extremely fine hole patterns. Here we ascribe the uniform deposits associated with cosolvents to a hybrid self-assembly process. The cosolvent drop segregates during evaporation, resulting in an elevated concentration of higher vapor pressure solvent at the drop surface.[10] Consequently, the particles, miscible only in the higher vapor pressure solvent, are carried toward the drop surface. Once at the drop surface, the particles self-assemble due to attractive particle−interface interactions.[11,12] Real-time observations during evaporation reveal the mechanisms of this self-assembly process. The observed drop profile kinetics agree well with our evaporation model for cosolvent drops. We also show that film uniformity depends on an optimal initial particle concentration, below which results in voids and above which exhibits a coffee ring formation. Moreover, this technique is used to produce thin film devices such as flexible broadband neutral density filters and semitransparent mirrors. This hybrid self-assembly approach requires no particle−substrate interactions, is scalable, robust, and transferrable. In essence, this work reveals the mechanism for co-solvent-based uniform deposits and demonstrates applications for drop-based fabrication of thin film devices.

This paper describes a process that is applicable to any cosolvent system where the dispersed particles (or nonvolatile material, in general) are miscible only in the solvent with a higher vapor pressure. However, the scope of this study is focused specifically on a system composed of an ethanol/water cosolvent mixture, which has been well-studied,[10,13−15] and thiol-capped Ga−In nanoparticles (see Figure 1a), a recently characterized class of nanoparticles.[16,17] The process is transferable to any substrate on which there is contact line pinning throughout evaporation; however, for this study we focus our results on polydimethylsiloxane (PDMS) substrates. We found substantially varying deposit outcomes with other control groups (see Supporting Information Figures S1 and S2). Single-solvent (ethanol only) drops exhibited various particle size-dependent structures, including distributed clumps for large particles (268 ± 51 nm), highly pronounced coffee rings for medium particles (110 ± 22 nm), or less pronounced

Received: December 27, 2015
Accepted: March 23, 2016
Published: March 23, 2016

DOI: 10.1021/acsami.5b12687
ACS Appl. Mater. Interfaces 2016, 8, 34171−34178

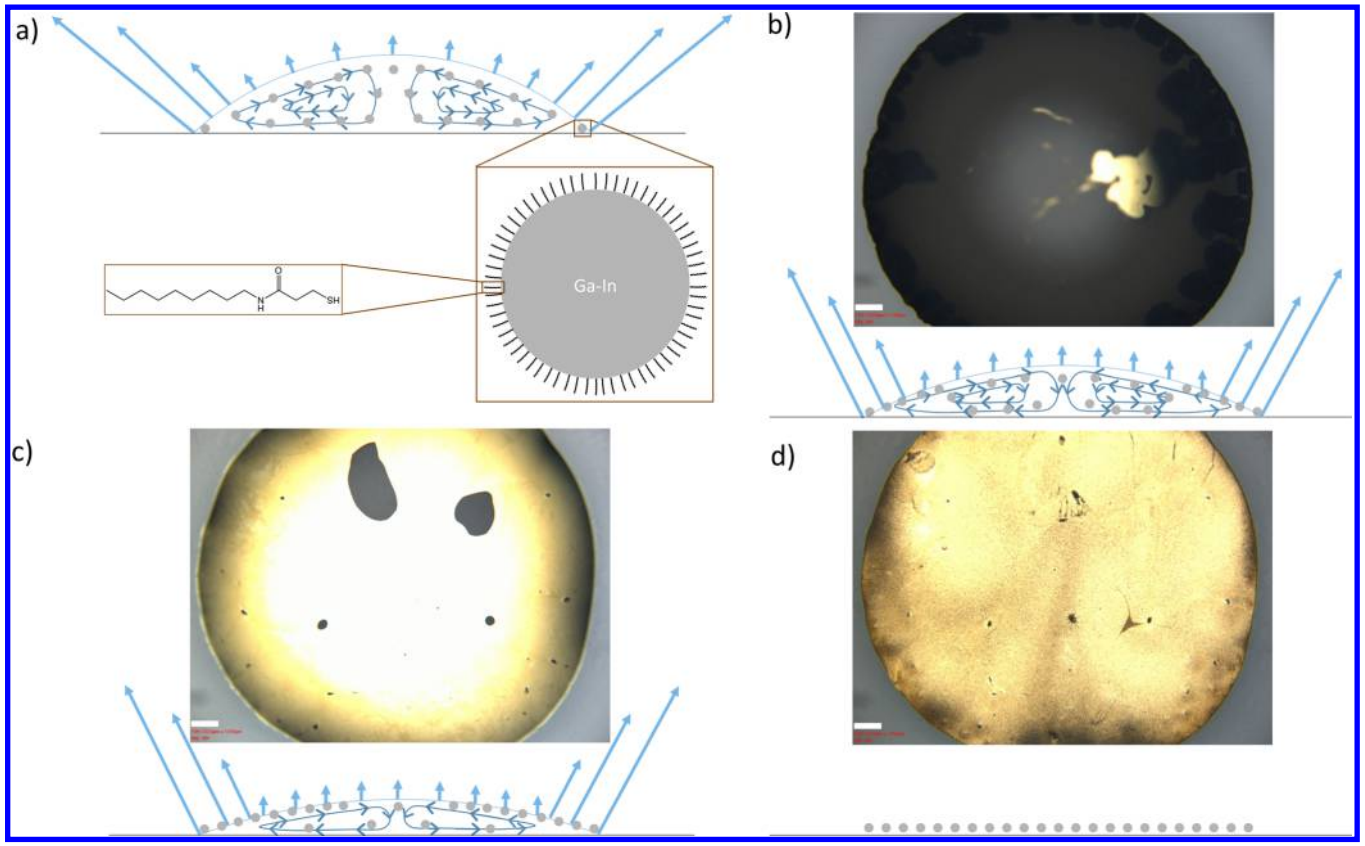

Figure 1. Self-assembly process. (a) Multiscale schematic of drop at the onset of evaporation including a macroscale depiction of the drop with nanoparticles uniformly dispersed throughout, a nanoscale representation of a single nanoparticle covered with a self-assembled monolayer of thiol, and a molecular-scale diagram of the chemical structure of the thiol. (b–d) Representative top view micrographs and corresponding side view schematics of self-assembly process at (b) an early stage of evaporation (<10% of evaporation time), (c) middle stage of evaporation (50% of evaporation time), and (d) deposit after evaporation. Arrows drawn at surface of drop represent a simplified depiction of the evaporative flux. Arrows drawn inside drop display a cartoon of internal streamlines induced by evaporation and surface tension gradients. Scale bars are 150 μm in length.

outer coffee rings with interior fractal-like deposits for small particles (84 ± 18 nm). We note that fractal patterns were observed at the contact line for single-drops containing all particle sizes (see Figure S1). With the inclusion of a lower vapor pressure solvent (water in this case), the resulting deposit structures became strikingly uniform, ranging from thick, in the cases where the contact line becomes depinned early during the evaporation process (see Figure S2), to extremely thin, when the contact line remains pinned throughout evaporation. This study focuses on the latter case.

Figure 1 shows the self-assembly process for particle monolayers via coevaporation dynamics (see also S1). Note that the areas of assembled particles appear visually bright with slight color differences due to light scattering from the curvature of the drop surface. As evident from Figure 1b, assembly begins at the onset of evaporation when a ring of nanoparticles nucleates at the contact line. This is expected, because particles within evaporating drops will tend toward the surface where evaporation flux is the highest.[1,18] Following nucleation, rather than further accumulation of nanoparticles at the boundary to form a previously observed coffee ring,[1] the structure transitions into a uniform sheet over the surface of the drop (Figure 1b) as the surface area is reduced and more nanoparticles are introduced to the interface. Note that the Marangoni flow within the drop during evaporation recirculates nanoparticles below the surface until they are introduced to the interface.

The direction of the Marangoni flow can be deduced by considering the influence of gradients in temperature, ethanol concentration, and nanoparticle concentration on surface tension gradients. A detailed discussion and relevant calculations are included in Section 1 of the Supporting Information; however, we include a brief overview here. The Marangoni flow may be either thermally driven or concentration driven, where the dominant case dictates the direction of the internal droplet flow. The mismatch in thermal conductivities between the substrate and the liquid indicates a Marangoni flow from the top of the drop to the bottom along the liquid–air interface and from the contact line toward the center of the drop along the liquid–solid interface (opposite of what is depicted in Figure 1) and a corresponding thermal Marangoni number, $Ma_T = 5.18 \times 10^3$. On the other hand, given the higher evaporation rate of ethanol compared to water, it is expected that there will be an elevated concentration of ethanol at the contact line where the flux is the highest. Because ethanol also has a lower surface tension, this results in a concentration driven surface tension gradient opposing the thermally driven gradient and a flow opposing the one brought about by thermal gradients (in the same direction as that depicted in Figure 1). The magnitude of the concentration driven Marangoni number associated with the gradients in ethanol concentration is $Ma_C = 1.53 \times 10^7$, which is 4 orders of magnitude larger than Ma_T and therefore dominates the direction of the flow. Moreover, the influence of the nanoparticles can further contribute to this flow in two

DOI: 10.1021/acsami.5b12687
ACS Appl. Mater. Interfaces 2016, 8, 34171–34178

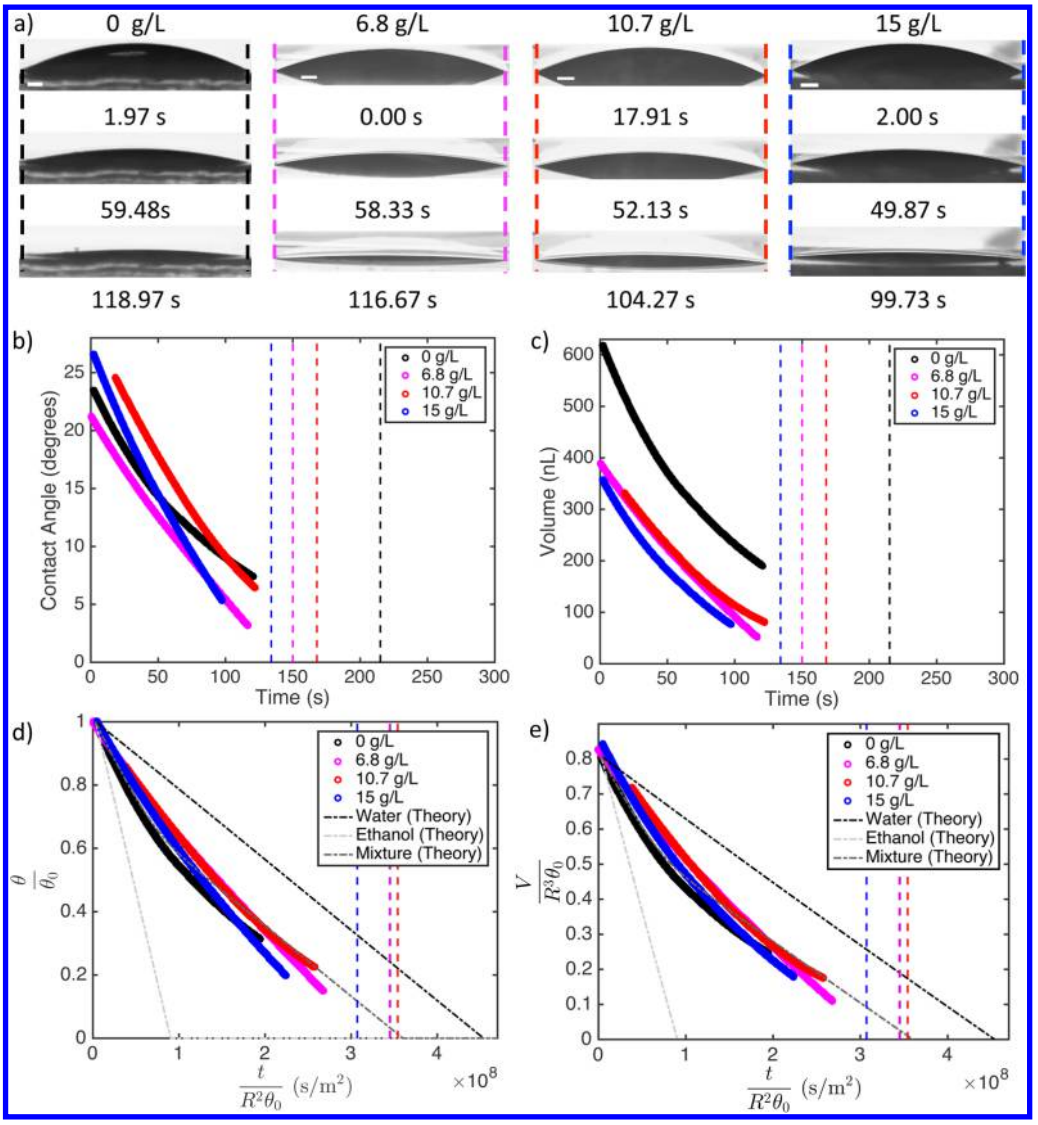

Figure 2. Evaporation process. (a) Profile images of sessile drops with various particle concentrations at different times (beginning, middle, end) during the evaporation process. Vertical dashed lines are used to highlight that the drops remain pinned (i.e., constant contact radius) throughout this process. Concentrations are given in grams/liter (g/L). Scale bars are 150 μm in length. (b–e) Kinetics of drop geometry during evaporation, including (b) contact angle, (c) volume, (d) dimensionless contact angle plotted with respect to time normalized by drop size and initial contact angle, and (e) dimensionless volume with respect to time normalized by drop size and initial contact angle. Vertically oriented dashed lines mark the total evaporation time for each experiment. The theory curves were generated based on observed initial conditions for the 0 g/L drop experiment (see Section 2 of SI). For reference, the particles for the deposits in this figure had a mean size of 268 nm with a standard deviation of 51 nm (see Experimental Section and Figure S4).

ways. First, the areas of the drop surface that are densely packed with nanoparticles (initially at the contact line) will exhibit a lower surface tension compared to areas that are particle free (see Figure S3), resulting in a surface flow from the edge of the drop to its center along the liquid–air interface. Second, the nanoparticles can be viewed effectively as surface contaminants, which can further reduce Ma_T by as much as 2 orders of magnitude,[19] thus increasing the relative dominance of the concentration driven flow.

The monolayer growth at the drop surface continues throughout the evaporation process until the higher vapor pressure solvent has completely evaporated and all of the particles have reached the interface (Figure 1c). During the final stages of the evaporation process, the contact line of the evaporating fluid depins, allowing for the assembled sheet of nanoparticles to collapse onto the substrate (Figure 1d). These observations suggest a process qualitatively different from previously reported methods for producing uniform films from evaporating drops, which solely employ interparticle capillary interactions,[20] particle–interface interactions,[21] or fluid–particle interactions.[19,22] Instead, this assembly process appears to be a hybrid case wherein particle–fluid interactions carry the particles to the boundary, followed by particle–interface interactions that assemble the particles into a sheet at the surface of the drop. Moreover, we observed sheet fracturing (see S1, 0:27–0:35) in drops with low particle loading and sheet buckling (see S2, 1:18–1:53) in drops with high particle loading, similar to that seen in evaporating drops containing latex particles.[23] This observed mechanical behavior of the sheet (i.e., fracturing of sheets in tension associated with drops with low particle loading and buckling of sheets in compression

DOI: 10.1021/acsami.5b12687
ACS Appl. Mater. Interfaces 2016, 8, 34171–34178

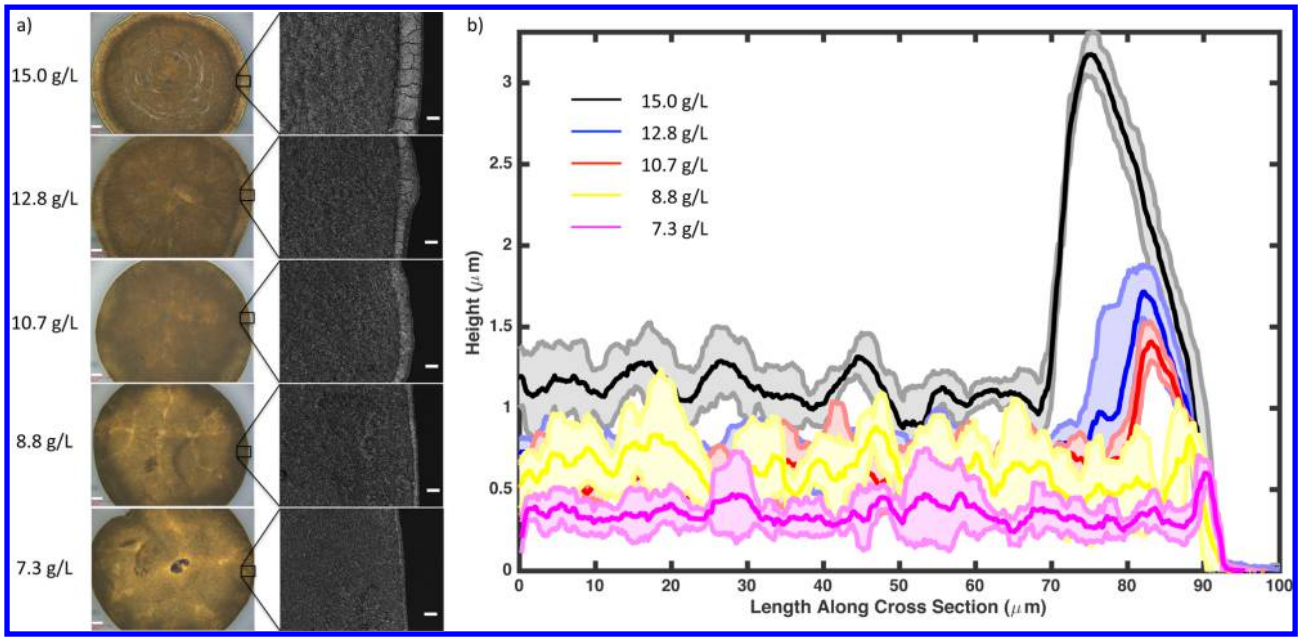

Figure 3. Tuning particle concentration eliminates coffee ring. (a) Optical micrographs (left) of deposits left behind (scale bars are 150 μm in length) with corresponding detail confocal intensity micrographs (right) of the deposit edge (scale bars are 10 μm in length). (b) Corresponding profiles at edge of deposits. Solid lines represent average profile. Lighter shaded regions represent one standard deviation (n = 5) above and below the average profile. For reference, the particles for the deposits in this figure had a mean size of 268 nm with a standard deviation of 51 nm (See Experimental Section and Figure S4).

associated with drops with high particle loading) is indicative of a solid-like nanocrystal.

Evaporation studies were conducted to reveal further the two mechanisms of this self-assembly process, as summarized in Figure 2. Figure 2a shows profile images of cosolvent sessile drops with various particle concentrations throughout the evaporation process. As evident from Figure 2b–e, the evaporation dynamics initially favor that of pure ethanol despite the fact that the initial concentration of water is much larger (initial mole fractions of water and ethanol within the drop are $x_w \approx 0.87$ and $x_e \approx 0.13$, respectively), which supports the previous experimental observation that the drop rapidly segregates during evaporation into an outer ethanol shell and a water enriched core.[10] The evaporation process can be modeled as quasi-steady state, where liquid vapor equilibrium applies (see Sections 2.1–2.3 of SI for a more detailed discussion on how the evaporation process is modeled). In contrast to previous studies on evaporating drops of ethanol–water mixtures,[10] our model accounts for the azeotropic effect (see Section 2.4 of SI). As seen in Figure S5, the vapor mole fraction of ethanol just above the drop surface, y_e, is significantly larger than the liquid mole fraction of ethanol within the drop (e.g., initially for this study $x_e \approx 0.13$ and $y_e \approx 0.49$). To maintain this condition, an excess of ethanol must be present at the interface. Moreover, the larger evaporation rate of ethanol during this process (see Figure S6b) amplifies the transport of the ethanol to the surface. Because it is known that the thiol-capped nanoparticles form stable colloidal suspensions in ethanol[16,17] and are also hydrophobic[24] (see also Figure S3), they migrate to the drop surface via the evaporating ethanol due to fluid–particle interactions, completing the first part of the assembly process. Once at the interface between the water enriched core and the ethanol shell, it is expected that the nanoparticles assemble due to particle–interface interactions,[11,12] thereby concluding the second phase of the hybrid self-assembly process.

We also examine the effects of particle concentration on the evaporation process (note that nanoparticle concentrations here are reported per volume of total solution). Figure 2a shows that the drops remained pinned throughout most of the evaporation process, regardless of particle loading (see also Figure S7). Moreover, Figure 2b shows similar initial contact angles among all concentrations, indicating that the wetting behavior is dominated by the interaction between the solvent mixture and the substrate. Normalizing the data from Figure 2b,c to account for differences in drop size and shape (see Section 2.5 of SI for normalization description) enables comparisons between our cosolvent evaporation model and drops of various particle loadings. These normalization results are shown in Figure 2d,e. Note that this normalization is applicable for evaporating drops with contact angles that are less than 45°,[25] which is applicable to our system. After accounting for differences in drop size and shape, the dynamics appear to behave in accordance with that predicted from our mixture evaporation theory, indicating that particle concentration has little effect on the evolution of the drop profile during evaporation throughout a majority of the drop lifetime. Moreover, the low model errors (<5%) in the normalized total evaporation time for low particle concentrations (<15.0 g·L^{-1} or <2.38 × 10^{14} particles·L^{-1} or <0.24 vol %) also indicate a good model fit toward the end of the evaporation process. However, there is a relatively large discrepancy (≈17% model error) for the high particle concentration (15.0 g·L^{-1} or 2.38 × 10^{14} particles·L^{-1} or 0.24 vol %). This indicates that the model is valid over a reasonable range of concentrations (≤10.7 g·L^{-1} or ≤1.70 × 10^{14} particles·L^{-1} or ≤0.17 vol %), but should be augmented to account for the effects of the particles at high concentrations (≥15.0 g·L^{-1} or ≥2.38 × 10^{14} particles·L^{-1} or ≥0.24 vol %).

DOI: 10.1021/acsami.5b12687
ACS Appl. Mater. Interfaces 2016, 8, 34171–34178

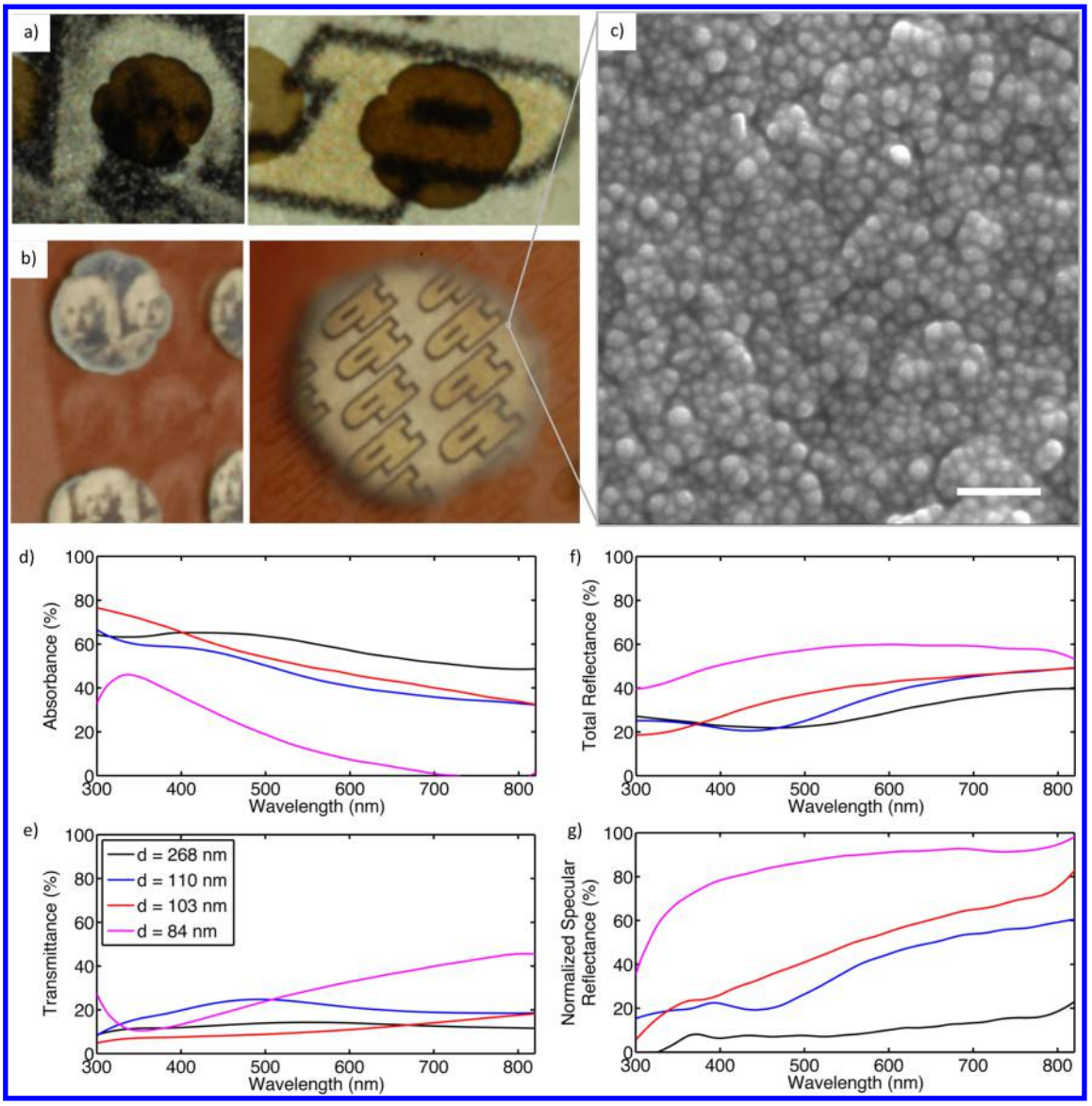

Figure 4. Application to thin film optics. (a–b) Qualitative examples demonstrating use of deposits as thin film devices. (a) Filters, where the deposit reduces the amount of light transmitted through (left) a close-up image of Einstein and (right) a close-up image of a Purdue "P". (b) Mirrors, where the deposit reflects light incident on (left) an image of an array of Einsteins and (right) an image of an array of Purdue "P's". Deposits are approximately 2 mm in diameter. (c) Representative SEM image of deposit morphology for the 84 ± 18 nm samples used in panels a and b (scale bar is 500 nm in length). (d–g) Spectrophotometry data for samples of various particle size including (d) absorbance, (e) transmittance, (f) reflectance, and (g) specular reflectance normalized by total reflectance.

Figure 3 summarizes the influence of initial particle concentration on the final morphology of the deposit. Deposits with high initial concentrations (15.0 g·L^{-1} or 2.38 × 10^{14} particles·L^{-1}) exhibit a dense accumulation of particles at the boundary (i.e., a large coffee ring), with a uniform deposit at the interior of the drop. Note the presence of cracks in the coffee ring of the high concentration deposit, indicative of high particle loading in dry colloidal deposits.[17] As evident from Figure 3, reducing the initial concentration results in thinner thickness of the uniform interior of the deposit as well as a size decrease of the coffee ring, with a complete elimination corresponding to concentrations <8.8 g·L^{-1} (1.40 × 10^{14} particles·L^{-1}). Small voids in the deposit at the smallest initial concentration (7.3 g·L^{-1} or 1.16 × 10^{14} particles·L^{-1}) suggest that the optimal initial concentration that will result in a uniform monolayer deposit lies between 7.3 and 8.8 g·L^{-1}. This range can be transformed to the number of particles in a drop (n) under the spherical cap approximation (see Section 2.1 of SI for validation of this approximation) via $n = 2cR^3(1 + \cos(\theta_0))^2(2 + \cos(\theta_0))/d^3\rho \sin^3(\theta_0)$; where c is the initial mass concentration of particles, R is the areal contact radius of the deposit, θ_0 is the contact angle of the drop at the onset of evaporation, d is the particle size, and ρ is the mass density of the particle. Substituting in appropriate values for these experiments: 7.3 g·L^{-1} < c < 8.8 g·L^{-1}, $R \approx 1.2$ mm, $\theta_0 \approx 25°$, $\rho = 6250$ kg·m^{-3}, and $d = 268$ nm (the particle size used for the study in Figure 3), results in an optimal number of particles in a drop to be between 7.1 × 10^7 and 8.5 × 10^7. Theoretically, a closely packed monolayer of particles from a deposited drop requires $n_{optimal} = 4pR^2d^{-2}$, where $p \approx 0.907$ is the hexagonal packing factor for circles in a plane.[26] We assume hexagonal packing because the time scale for the particles to

DOI: 10.1021/acsami.5b12687
ACS Appl. Mater. Interfaces 2016, 8, 34171–34178

assemble by particle diffusion is found to be smaller than the time scale for the particles to reach the drop surface due to evaporation (see Section 3 of the SI), indicating that the likely arrangement of the particles at the surface is hexagonal packing.[27,28] Therefore, the theoretically estimated number of particles per drop to produce uniform monolayer deposits is $n_{optimal} = 7.3 \times 10^7$ (corresponding to an optimal concentration of $c_{optimal} = 7.5\ g{\cdot}L^{-1}$), which indeed falls within our observed range. This demonstrates a process for determining appropriate particle concentrations for uniform monolayer deposits in cosolvent formulations.

On the other hand, these results also indicate that exceeding the appropriate concentration range will result in the formation of a coffee ring at the contact line and an increase in thickness over the uniform interior of the deposit, which is expected due to the nature of monolayer growth during evaporation. Once a monolayer is achieved during evaporation, any particles remaining within the drop will begin to form multilayer structures as they move to the surface and collide with particles within the formed monolayer. The likelihood for collisions is largest at the edge of the drop because this is where the radial velocity is highest,[19] resulting in the presence of coffee ring deposits for $c > c_{optimal}$, as shown in Figure 3. Note the appearance of gray spots in the optical micrographs of Figure 3a for $c > c_{optimal}$. These gray spots in the optical microscope images of the deposits are a result of differences in light scattering, indicating differences in local film thickness (lower local thicknesses in the gray areas). We suspect that this is a result of multiple layers being formed throughout areas of surface while the first layer is still being formed in others.

Experiments were conducted to demonstrate application of this self-assembly process to the fabrication of high performance drop-on-demand thin film optical devices, summarized in Figure 4. Figure 4a,b qualitatively highlights drop-deposited devices such as filters and mirrors. The representative scanning electron micrograph in Figure 4c reveals that these deposits are uniform and densely packed throughout. Figure 4d–g shows the measured optical results for self-assembled deposits of various nanoparticle size. The larger particles will produce thicker samples, resulting in an increased absorbance, as seen in Figure 4d. This gives rise to the reverse effect for the transmittance (see Figure 4e). The absorbance and transmittance spectra also flatten with increased particle size. This may be due to the increased size heterogeneity with respect to particle size (see Figure S4), allowing for cancellation of resonance peaks associated with different sized particles within the sample. Most notable of this effect is the flat transmission response (13% ± 2%) associated with the largest particle (d = 268 nm) monolayer deposits over the entire sampled range (300–820 nm), which demonstrates an application of these deposits as a broadband neutral density filter. As shown in Figure 4f,g, the samples are also inherently reflective given their metallic composition. The decrease in particle size gives rise to smoother deposits. As the deposits become smoother, their total and specular reflectances increase, resulting in the trend we see here. Regarding application, as shown in Figure 4g, the high specular reflectance response (>80%) associated with the small particle (d = 84 nm) deposits shows promise for use as a mirror, especially for wavelengths in the visible–near-infrared range. These results are remarkable considering the flexing and stretching experienced by the samples during optical measurement preparation (see Experimental Section).

Our experiments have revealed that uniform deposits from evaporating cosolvent drops are created by a hybrid of two self-assembly mechanisms: (1) fluid–particle interactions, where the nanoparticles are carried to the drop surface by the higher vapor pressure solvent, followed by (2) particle–interface interactions once the particles reach the interface of the phase-segregated drop. As observed, this assembly process occurs at the surface of the drop, indicating independence of this mechanism with respect to substrate. The cosolvent evaporation model we have developed accurately describes the drop profile kinetics and could be used for future design of cosolvent-based functional inks. The agreement of the size and shape normalized data and model show scalability of this process. Our results also show a simple means for designing particle concentrations to produce uniform monolayers. Moreover, we demonstrate the application of cosolvent formulation to high performance drop-on-demand thin film devices such as mirrors and broad band neutral density filters. Given these results, it is likely that high throughput drop deposition methods (e.g., roll-to-roll inkjet printing) will receive more attention as a viable means to fabricate thin film devices in the future.

EXPERIMENTAL SECTION

Preparation of EGaInNP Dispersions. EGaInNP dispersions were prepared by an ultrasonication method similar to previous works.[16,17] All samples were prepared in 3 dram bottles (Kimble Chase). Before ultrasonication the vials were thoroughly washed with Liquinox detergent (Alconox), followed by a rinse with distilled water, followed by a rinse with ethanol to remove surface impurities. Once clean, a nominal mass of 1 g of eutectic Gallium–Indium alloy (EGaIn) (Sigma-Aldrich) was added to the vial via syringe. Masses were measured using a Ohaus Pioneer balance with 0.1 mg resolution. This was followed by the addition of 120 μL (Labnet BioPette, 1000 μL size) of 100 mM solution of 3-mercapto-*N*-nonylpropionamide (1ATC9, Sigma-Aldrich). An additional 3880 μL of pure ethanol was added to achieve a final thiol concentration of 3 mM and final liquid volume of 4 mL. Once the sample was prepared, the liquid metal was dispersed into the solvent using a Qsonica Q700 probe ultrasonicator fitted with a 1/16 in microtip. The vial with EGaIn and solvent was contained in a water bath to prevent overheating and evaporation of the sample. The sample was sonicated for 1 h at an amplitude of 30%. After sonication, samples were either further processed via centrifugation or placed in a −35 °C freezer for later processing.

Differential centrifugation was used to separate particles of various sizes. The process is as follows. Sonicated samples were distributed evenly into 1.5 mL polypropylene centrifuge tubes, lightly bath-sonicated (Branson 1800) in isopropyl alcohol (Macron Fine Chemicals) for approximately 20 s, and placed in a refrigerator at approximately 10 °C for several minutes to allow the samples to reach below the melting point of the bulk alloy. The samples were then rinsed of any free thiol by centrifugation (RevSpin RS-200). Namely, the samples were spun at 10,000 rotations per minute (RPM) (5529 relative centrifugal force (RCF)) for 10 min. The resulting aliquots were discarded and the pellets were resuspended via light sonication in ethanol. This process was repeated three times to ensure there was no unbound thiol in the samples. Next, the resuspended pellets were spun at 2,000 rpm (220.5 RCF) for 10 min. The aliquots from this step were poured into centrifuge tubes to obtain smaller particles, whereas the pellets were resuspended via light sonication in fresh ethanol. This process was repeated three times. This procedure was further applied to the aliquots to obtain particles at 4,000, 6,000, and 8,000 rpm (884, 1990, and 3537.5, RCF, respectively) in series. Samples from each differential centrifugation condition were drop deposited on clean Si for scanning electron microscope (SEM)-based particles sizing (see Figure S4). Ethanol/water mixtures were made by adding a known volume (Lagnet BioPette, 20 μL) of ethanol to a pellet of dried

DOI: 10.1021/acsami.5b12687
ACS Appl. Mater. Interfaces 2016, 8, 34171–34178

particles, followed by light bath sonication for resuspening, followed by the addition of the appropriate volume (Lagnet BioPette, 20 μL) of distilled water to reach the required mixture ratio (for this study an ethanol mass fraction of ≈28% was used).

Preparation of Substrates. The polydimethylsiloxane (PDMS, Sylgard 184, Dow Corning) samples were prepared as follows. The polymer is provided as a two-part system consisting of a base and a curing agent. The two liquids are mixed in a 10:1 mass ratio. The two parts were mixed by hand and placed in THINKY ARE 310 orbital mixer for further mixing and degassing. Once mixed, the liquid polymer was cast onto 2 in. × 3 in. borosilicate glass slides using a Specialty Coating Systems Spin-coat G3-8 spin coater at 200 rev·min^{-1} for 60 s. Coated slides were cured in an incubator at 60 °C for at least 4 h. Upon curing, the polymer film was cut into 0.25 in squares, and cleaned by sonication in acetone, followed by rising with acetone, isopropyl alcohol, ethanol, and water. The rinsed samples were then dried with compressed air. PDMS squares were removed from the diced sample and placed on a clean glass carrier slides for plasma treatment. Slides were treated with oxygen plasma (Plasma Etch Venus 25 plasma etcher) for 5 min at 50 W with an oxygen flow rate of 10 CFM·min^{-1}. Treated surfaces were used within 24 h to maintain consistent drop wetting and contact line pinning behavior (see Figure S8). The Si substrates employed for drop-depositing monolayers (see Figure S9) were prepared using a procedure described elsewhere.[29] Once received, they were cleaned via bath sonication in acetone, isopropyl alcohol, then ethanol, for 5 min each, drying with air after each sonication treatment.

Drop Evaporation Experiments. All drop evaporation experiments were conducted at room conditions with a measured temperature (Fluke 87 V with K-type thermocouple) of 23 ± 2 °C and a measured relative humidity (Kele HS-2000D) of 21% ± 2%. Typical experiments for conducting drop evaporation were conducted as follows. Sessile drops were formed by gently placing small volumes of colloidal dispersion (see previous Experimental Subsections) via pipette (Lagnet BioPette, 20 μL) onto stationary substrates located on a microscope stage (Zeta 20 with custom tilt attachment). The substrates employed for observing the evaporation process were plasma treated PDMS (see Preparation of Substrates). Upon deposition of drops, top and side views were filmed from the optical microscope with a screen capture software (Camtasia 8). Using an in-house MATLAB image analysis script, the geometry of the profiles were analyzed throughout the evaporation process until the profile became too small for the script to detect (between 4° and 9°, depending on initial drop size, objective, and focusing conditions). Drop deposits were also made on Si substrates (representative results shown in Figure S9).

Deposit and Particle Characterization. Samples for particle size characterization were prepared by depositing small volumes of each differential centrifugation condition via micropipette (Lagnet BioPette, 20 μL) onto clean Si substrates. SEM images of these samples were then obtained (Philips XL-40 FEI). All images were analyzed using previously reported procedure[17] (results from this process can be found in Figure S4). Topography measurements of the self-assembled deposits on PDMS substrates were obtained using a confocal microscope (LEXT 3000) with a 100× microscope objective. The PDMS squares were then mechanically peeled from the carrier glass slide and placed onto smaller glass slides for spectrophotometry measurements (PerkinElmer Lambda 950, light scan from 300 to 820 nm, with a resolution of 0.5 nm and a 5 s dwell time). Following topography and spectrophotometry measurements, the self-assembled deposits on PDMS were prepared for SEM (FEI Nova nanoSEM FESEM) imaging (representative result shown in Figure 4c) via platinum sputtering (Cressington 208 HR, 40 mA, 0.08 mbar for 60 s). Self-assembled drop deposits were also placed on Si substrates using the same method as the drop evaporation experiments and imaged via SEM (FEI Quanta 2D FEG Dual-beam SEM) (result shown in Figure S9).

Langmuir Trough Experiments. The instrument used in this work is a Kibron microtrough with a pair of automated movable barriers, which compresses the nanoparticles that are spread on a water surface, and a surface pressure sensor, which controls the barriers.[30] Monolayers of EGaINPs were prepared using a spreading ethanolic solution with a concentration of 50 mg·mL^{-1}. The sample was spread carefully using a positive displacement pipette at a rate of ≈0.6 μL·s^{-1}. After the solvent evaporated, the hydrophobic dodecanethiol (1ATC9)-stabilized EGaInNPs remained on the water surface, appearing as a shiny silver color (see Figure S3), and were then compressed by moving the barriers at a speed of 10 mm·min^{-1}. The surface pressure isotherm was recorded throughout the compression. The temperature of the double deionized water (18 MΩ·cm in the trough) was about 20 °C.

■ ASSOCIATED CONTENT

Supporting Information

The Supporting Information is available free of charge on the ACS Publications website at DOI: 10.1021/acsami.5b12687.

Summary table of model parameters; discussions on Marangoni flow direction, theory and model for cosolvent evaporation (including model assumptions, thermal and convective effects, mixture considerations, and normalization of parameters), and diffusive time scale versus hydrodynamic time scale; figures showing SEM image of fractal patterns, optical images of deposit outcomes for varied solvent formulations and substrate treatments, Langmuir trough experimental results, process for obtaining particle sizes, vapor−liquid equilibrium data for ethanol−water mixtures, model predictions for drop mass and composition dynamics, observed contact radius during evaporation, postplasma time effects on drop wetting and contact line pinning, and demonstration of monolayer via the hybrid self-assembly process (PDF).

Movie S1, showing the hybrid self-assembly process (MOV)

Movie S2, showing the shell buckling for drops with high concentrations of nanoparticles (MP4)

■ AUTHOR INFORMATION

Corresponding Authors

*J. W. Boley. E-mail: jwboley@seas.harvard.edu.

*R. K. Kramer. E-mail: rebeccakramer@purdue.edu.

Present Address

[§]John A. Paulson School of Engineering and Applied Sciences, Harvard University, Cambridge, Massachusetts 02138, United States

Notes

The authors declare no competing financial interest.

■ ACKNOWLEDGMENTS

This work was partially supported by an Early Career Faculty grant from NASA's Space Technology Research Grants Program (NNX14A052G). E.L.W. is supported under the National Science Foundation Graduate Research Fellowship program (DGE-1333468). The authors thank Professor Vladimir Shalaev for providing access to the spectrophotometer equipment and Dr. Alexei Lagoutchev for training on the spectrophotometer.

■ REFERENCES

(1) Deegan, R. D.; Bakajin, O.; Dupont, T. F.; Huber, G.; Nagel, S. R.; Witten, T. A. Cxapillary Flow as the Cause of Ring Stains from Dried Liquid Drops. *Nature* **1997**, *389*, 827−829.

DOI: 10.1021/acsami.5b12687
ACS Appl. Mater. Interfaces 2016, 8, 34171−34178

(2) Kaya, D.; Belyi, V. A.; Muthukumar, M. Pattern Formation in Drying Droplets of Polyelectrolyte and Salt. *J. Chem. Phys.* **2010**, *133*, 114905.
(3) Mougin, K.; Haidara, H. Complex Pattern Formation in Drying Dispersions. *Langmuir* **2002**, *18*, 9566−9569.
(4) Tekin, E.; de Gans, B.-J.; Schubert, U. S. Ink-jet Printing of Polymers - from Single Dots to Thin Film Libraries. *J. Mater. Chem.* **2004**, *14*, 2627−2632.
(5) Park, J.; Moon, J. Control of Colloidal Particle Deposit Patterns within Picoliter Droplets Ejected by Ink-Jet Printing. *Langmuir* **2006**, *22*, 3506−3513.
(6) Kong, Y. L.; Tamargo, I. A.; Kim, H.; Johnson, B. N.; Gupta, M. K.; Koh, T.-W.; Chin, H.-A.; Steingart, D. A.; Rand, B. P.; McAlpine, M. C. 3D Printed Quantum Dot Light-Emitting Diodes. *Nano Lett.* **2014**, *14*, 7017−7023.
(7) Cui, L.; Li, Y.; Wang, J.; Tian, E.; Zhang, X.; Zhang, Y.; Song, Y.; Jiang, L. Fabrication of Large-Area Patterned Photonic Crystals by Ink-jet Printing. *J. Mater. Chem.* **2009**, *19*, 5499−5502.
(8) Janoschka, T.; Teichler, A.; Häupler, B.; Jähnert, T.; Hager, M. D.; Schubert, U. S. Reactive Inkjet Printing of Cathodes for Organic Radical Batteries. *Adv. Energy Mater.* **2013**, *3*, 1025−1028.
(9) Hoth, C.; Choulis, S.; Schilinsky, P.; Brabec, C. High Photovoltaic Performance of Inkjet Printed Polymer:Fullerene Blends. *Adv. Mater.* **2007**, *19*, 3973−3978.
(10) Fang, X.; Li, B.; Wu, J.; Maldarelli, C.; Sokolov, J. C.; Rafailovich, M. H.; Somasundaran, P. Imaging and Estimating the Surface Heterogeneity on a Droplet Containing Cosolvents. *J. Phys. Chem. B* **2009**, *113*, 9636−9639.
(11) Santhanam, V.; Liu, J.; Agarwal, R.; Andres, R. P. Self-Assembly of Uniform Monolayer Arrays of Nanoparticles. *Langmuir* **2003**, *19*, 7881−7887.
(12) Lin, Y.; Skaff, H.; Emrick, T.; Dinsmore, A. D.; Russell, T. P. Nanoparticle Assembly and Transport at Liquid-Liquid Interfaces. *Science* **2003**, *299*, 226−229.
(13) Hopkins, R. J.; Reid, J. P. Evaporation of Ethanol/Water Droplets: Examining the Temporal Evolution of Droplet Size, Composition and Temperature. *J. Phys. Chem. A* **2005**, *109*, 7923−7931.
(14) Liu, C.; Bonaccurso, E.; Butt, H.-J. Evaporation of Sessile Water/Ethanol Drops in a Controlled Environment. *Phys. Chem. Chem. Phys.* **2008**, *10*, 7150−7157.
(15) Homer, C. J.; Jiang, X.; Ward, T. L.; Brinker, C. J.; Reid, J. P. Measurements and Simulations of the Near-Surface Composition of Evaporating Ethanol-Water Droplets. *Phys. Chem. Chem. Phys.* **2009**, *11*, 7780−7791.
(16) Hohman, J. N.; Kim, M.; Wadsworth, G. A.; Bednar, H. R.; Jiang, J.; LeThai, M. A.; Weiss, P. S. Directing Substrate Morphology via Self-Assembly: Ligand-Mediated Scission of Gallium-Indium Microspheres to the Nanoscale. *Nano Lett.* **2011**, *11*, 5104−5110.
(17) Boley, J. W.; White, E. L.; Kramer, R. K. Mechanically Sintered Gallium−Indium Nanoparticles. *Adv. Mater.* **2015**, *27*, 2355−2360.
(18) Hu, H.; Larson, R. G. Evaporation of a Sessile Droplet on a Substrate. *J. Phys. Chem. B* **2002**, *106*, 1334−1344.
(19) Hu, H.; Larson, R. G. Marangoni Effect Reverses Coffee-Ring Depositions. *J. Phys. Chem. B* **2006**, *110*, 7090−7094.
(20) Yunker, P. J.; Still, T.; Lohr, M. A.; Yodh, A. G. Suppression of the Coffee-Ring Effect by Shape-Dependent Capillary Interactions. *Nature* **2011**, *476*, 308−311.
(21) Bigioni, T. P.; Lin, X.-M.; Nguyen, T. T.; Corwin, E. I.; Witten, T. A.; Jaeger, H. M. Kinetically Driven Self Assembly of Highly Ordered Nanoparticle Monolayers. *Nat. Mater.* **2006**, *5*, 265−270.
(22) Harris, D.; Hu, H.; Conrad, J.; Lewis, J. Patterning Colloidal Films via Evaporative Lithography. *Phys. Rev. Lett.* **2007**, *98*, 148301.
(23) Pauchard, L.; Couder, Y. Invagination during the collapse of an inhomogeneous spheroidal shell. *Europhys. Lett.* **2004**, *66*, 667−673.
(24) Huang, S.; Minami, K.; Sakaue, H.; Shingubara, S.; Takahagi, T. Effects of the Surface Pressure on the Formation of Langmuir-Blodgett Monolayer of Nanoparticles. *Langmuir* **2004**, *20*, 2274−2276.
(25) Popov, Y. O. Evaporative Deposition Patterns: Spatial Dimensions of the Deposit. *Phys. Rev. E* **2005**, *71*, 036313.
(26) Segre, B.; Mahler, K. On the Densest Packing of Circles. *American Mathematical Monthly* **1944**, *51*, 261−270.
(27) Marín, A. G.; Gelderblom, H.; Lohse, D.; Snoeijer, J. H. Order-to-Disorder Transition in Ring-Shaped Colloidal Stains. *Phys. Rev. Lett.* **2011**, *107*, 085502.
(28) Marín, Á. G.; Gelderblom, H.; Susarrey-Arce, A.; van Houselt, A.; Lefferts, L.; Gardeniers, J. G. E.; Lohse, D.; Snoeijer, J. H. Building microscopic soccer balls with evaporating colloidal fakir drops. *Proc. Natl. Acad. Sci. U. S. A.* **2012**, *109*, 16455−16458.
(29) Raghunathan, N.; Nishida, E.; Fruehling, A.; Chen, W.; Peroulis, D. Arrays of Silicon Cantilevers for Detecting High-G Rapidly Varying Acceleration Profiles. *IEEE Sensors 2010*, Kona, HI, November 1−4, 2010; pp 1203−1206.
(30) Li, H.; Sachsenhofer, R.; Binder, W. H.; Henze, T.; Thurn-Albrecht, T.; Busse, K.; Kressler, J. Hierarchical Organization of Poly(ethylene oxide)-block-poly(isobutylene) and Hydrophobically Modified Fe2O3 Nanoparticles at the Air/Water Interface and on Solid Supports. *Langmuir* **2009**, *25*, 8320−8329.

NOTE ADDED AFTER ASAP PUBLICATION

This paper was published on the Web on April 1, 2016, with an incomplete Supporting Information file. The corrected version was reposted on April 26, 2016. Two Supporting Information movie files were added, and the corrected version was reposted on July 26, 2016.

DOI: 10.1021/acsami.5b12687
ACS Appl. Mater. Interfaces 2016, 8, 34171−34178